ACS APPLIED ENGINEERING MATERIALS

pubs.acs.org/acsaenm Article

Shaping of Porous CeO_2 Powders into Highly Active Catalyst Carriers

Elena Martín Morales,* Andreína Alarcón, Martí Biset-Peiró, Elena Xuriguera, and Jordi Guilera

Cite This: *ACS Appl. Eng. Mater.* 2023, 1, 1106−1115 Read Online

ACCESS | Metrics & More | Article Recommendations | Supporting Information

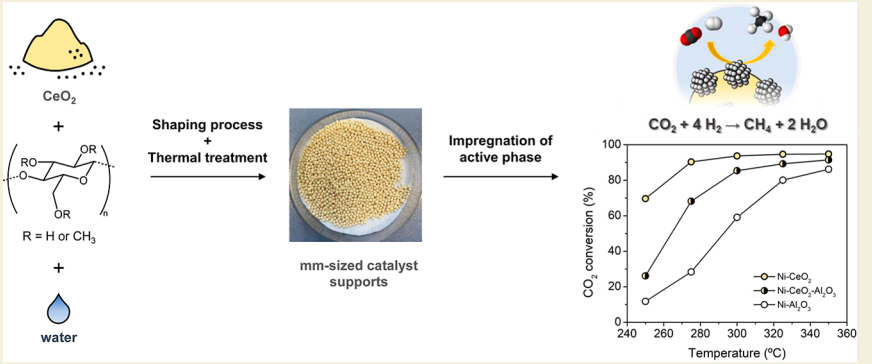

ABSTRACT: CeO_2 is attracting more and more attention because of its outstanding performance in heterogeneous catalysis, as an active support and a reaction promoter in reactions of industrial interest. We herein describe a novel and scalable manufacturing process of mm-sized CeO_2 spheres by a combination of extrusion and spheronization of CeO_2 porous powders. In this study, wet paste formulation and fabrication procedures were optimized, and as a result methylcellulose was identified as the best plasticizer for paste extrusion to provide well-defined spherical shapes and smooth surfaces, as well as reproducible batches. After nickel impregnation (10 wt %), the catalytic performance of CeO_2 supports was evaluated in the CO_2 methanation reaction (T = 250−350 °C, P = 5 bar·g) and compared with that of commercial Al_2O_3 spheres doped or not with CeO_2. These novel CeO_2-based catalysts are easily reduced at a moderate temperature and more active than the Al_2O_3 analogues, particularly at low reaction temperatures and small reactor volumes, properties that make their implementation in emerging reactor configurations very promising.

KEYWORDS: *cerium oxide, catalyst carrier, extrusion, spheronization, carbon dioxide methanation*

1. INTRODUCTION

CeO_2-based materials have gathered momentum in catalysis owing to the high activities obtained when used as supports and reaction promoters in several industrial applications.[1,2] The interest in CeO_2 over other metal oxides lies on its non-stoichiometric properties and the readiness to change between Ce(III) and Ce(IV) oxidation states while preserving its original structure, which allow the oxygen species to easily move across the CeO_2 lattice.[3] This ability to store and release oxygen can be considered responsible for the activation of catalytic substrates such as CO[4] or CO_2[5] and to facilitate the redox processes associated with the supported metal active species.[6] These unique properties explain the notable activities of CeO_2-based catalysts in reactions of high socioeconomic interest, such as the water gas shift reaction,[7] combustion of methane,[8] ammonia decomposition,[9] fuel oxidation in solid-oxide fuel cells,[10] or three-way catalysis,[11] among others. A reaction of special concern is the methanation of CO_2, a process in which ceria-based systems, in combination with catalytically active metals like nickel, have exhibited remarkable activities.[12−14]

CeO_2 in powder form, among other metal oxide supports, has been extensively studied at a molecular level in order to establish the structure−property relationships that govern the activity of heterogeneous catalysts. Powder catalysts, however, present critical limitations when implemented in real devices, such as the pressure drop or release of fine particles into the environment.[15] To overcome these undesired events in industrial applications, catalyst carriers are often presented in the form of pellets (mm-scale)[16] or monoliths (cm-scale),[17,18] which are easier to transport, manipulate, and recover after the operation. While monolithic bodies entail lower pressure drops, smaller structures like pellets accept higher metal loadings in an equivalent reactor volume.[19]

A common strategy for the shaping of powders into bigger bodies involves the use of agglomeration techniques such as

Received: November 20, 2022
Accepted: March 15, 2023
Published: March 29, 2023

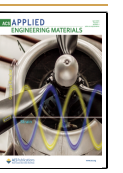

pelleting, granulation, or extrusion,[17,18] and more recently 3D-printing.[20,21] To achieve mild processing of the material, powders are typically mixed with water and other additives.[17,22] Gum guar,[23,24] cellulose derivatives,[25−27] or synthetic polymers[28] are recurring additives added to the formulations to tune their rheological behavior, thus enabling mild processing, and are commonly referred to as plasticizers. Acids and bases are used as peptizing agents to favor mixture homogeneity by changing the aggregation state of the powder particles.[22,29] Other additives can be introduced to obtain the desired physicochemical properties of the final materials. For instance, inorganic binders like clays,[30−32] silica,[32,33] and alumina,[25,32−34] are often employed to enhance the mechanical resistance of the shaped bodies.

The shaping of CeO_2 powders into bigger structures has been reported for solid-oxide fuel cell applications. For example, the fabrication of monolithic bodies by injection molding of a mixture of CeO_2 powder, ethylene-vinylacetate, paraffin wax, and stearic acid was studied.[35] Guesnet et al.[36] followed two different approaches to shape gadolinium-doped CeO_2 powders into 25 mm diameter disks: (a) a tape-casting process using additives like phosphate ester, dibutyl phthalate and synthetic polymers, and carbon particles as porogens and (b) die pressing associated with screen-printing. Similar to the latter, Llorca and co-workers[37] reported the compression of CeO_2 powders combined with polyvinyl alcohol into disks of 10 mm diameter using a uniaxial hydraulic press. Methods of shaping of CeO_2-based structures as catalyst supports for fixed-bed reactors have also been reported, such as the pelletization of porous CeO_2 powders previously impregnated with nickel salts into 0.25−0.5 mm pellets for CO methanation.[38] Extrusion methods have been employed as well to obtain cerium−zirconium mixed oxide cylindrical bodies of different compositions.[24,39] The shaped $Ce_{0.6}Zr_{0.4}O_2$ support in combination with the active metallic species exhibited high conversions in the trireforming of surrogate biogas.[23] Recently, monolithic CeO_2 structures with a woodpile arrangement have been attained out of a mixture of porous CeO_2 powders and concentrated HNO_3 by 3D-printing methods for the catalytic decomposition of ammonia.[40]

Among the different shaping techniques, the extrusion-spheronization technique allows the eventual variation of the pellet diameter to fit reactor specifications, for instance in microchanneled reactors, and the scale-up of the production to industrial amounts. For correct extrusion, pastes must have adequate rheological properties, determined by particle size and shape, liquid−solid ratio, and ionic occupation of particle surfaces.[41] Additives like polysaccharides and cellulose derivatives, polyethers, or polymeric alcohols can interact through hydrogen bonding with the hydroxyl surface groups of the CeO_2 particles, thus masking the morphology effects and allowing them to slide past each other when an extrusion force is applied.[42]

To the best of our knowledge, this study represents the first report of the fabrication of mm-sized CeO_2-based catalyst carriers using extrusion-spheronization with different extrusion-aid agents, and up to date, there are no commercially available mm-sized CeO_2-based catalysts. Three different extrusion-aid agents are evaluated, namely methylcellulose (MC), hydroxyethylcellulose (HEC), which have already been used in the fabrication of technical catalysts,[25,27] and polyvinylpyrrolidone (PVP), a polymer widely used as a particle dispersant.

As a proof of concept, the so-obtained CeO_2-based catalyst carriers were impregnated with nickel species and evaluated in the catalytic conversion of carbon dioxide into methane. The catalytic performance of the novel supports is hereby compared with that of commercial Al_2O_3 spheres, commonly used as catalyst supports.[43−45] Al_2O_3 spheres have been impregnated with Ni and Ni/CeO_2, respectively, to evaluate the best role of CeO_2, either as a promoter, as it has been typically used, or as a shaped support.

2. MATERIALS AND METHODS

2.1. Material Preparation

Cerium(III) nitrate hexahydrate, [$Ce(NO_3)_3{\cdot}6H_2O$] (99.5%, Alfa Aesar) was used for the synthesis of supports. Methylcellulose ($M_w \sim$ 14.000, Sigma), hydroxyethylcellulose ($M_w \sim$ 26.000, Sigma), and polyvinylpyrrolidone ($M_w \sim$ 40.000, Merck) were used as plasticizers. Nickel (II) nitrate hexahydrate [$Ni(NO_3)_2{\cdot}6H_2O$] (98%, Alfa Aesar) was used as a metal precursor. For comparison purposes, Al_2O_3 spheres were purchased from Norpro Saint-Gobain (d_p = 1 mm).

CeO_2 powder was synthesized by the calcination of $Ce(NO_3)_3{\cdot}6H_2O$ for 5 h at 500 °C (1 °C·min^{-1}). The solid thus obtained was then ball milled using a Retsch MM400 Oscillating mill. A wet mass was formed by mixing the CeO_2 powder with the plasticizer (1:0.055 dry mass ratio) and a predetermined volume of an aqueous 0.1 mM HNO_3 solution. The paste was homogenized for 20 min in a THINKY ARE-250 Conditioning Planetary Mixer. The pastes were extruded using a Caleva Multi-Lab Extruder (1 mm diameter, 55 rpm), and the extruded pellets were processed in a Caleva Multi-Lab Spheronizer (10−30 min, 2000 rpm). The resulting pellets were dried at 105 °C for 12 h and calcined at 500 °C for 4 h (5 °C·min^{-1}).

The CeO_2 carriers were impregnated with Ni by an incipient wet impregnation method to yield the Ni−CeO_2 catalyst with a Ni nominal content of 10 wt %. In a typical synthesis, 0.825 g of $Ni(NO_3)_2{\cdot}6H_2O$ were dissolved in 285 μL of deionized water. The precursor solution was then drop-casted over 1.5 g of CeO_2 catalyst carriers. The catalyst was dried at 105 °C for 12 h and calcined at 500 °C for 1 h (2 °C·min^{-1}). The reduced form of the catalyst was achieved by reduction under a hydrogen atmosphere (5% H_2 and 95% Ar, 100 mL·min^{-1}) at 350 °C 3 h (1 °C·min^{-1}).

In a similar procedure, commercial Al_2O_3 spheres were impregnated with a solution of 0.825 g of $Ni(NO_3)_2{\cdot}6H_2O$ in 1.05 mL of water to yield the Ni−Al_2O_3 catalyst. The Ni−CeO_2−Al_2O_3 catalyst was synthesized by co-impregnation of the Al_2O_3 spheres with 0.94 g of $Ni(NO_3)_2{\cdot}6H_2O$ and 0.47 g of $Ce(NO_3)_3{\cdot}6H_2O$ dissolved in 1.05 mL of water, aiming at Ni and CeO_2 nominal contents of 10 wt %. The CeO_2 promoter loading was selected following previous optimization studies.[46] The catalysts were then dried at 105 °C for 12 h and calcined at 500 °C for 1 h (2 °C·min^{-1}). Reduction of the Al_2O_3-based catalysts was performed under hydrogen atmosphere (5% H_2 and 95% Ar, 100 mL·min^{-1}) at 500 °C during 3 h (1 °C·min^{-1}).

2.2. Material Characterization

Scanning electron microscopy (SEM) micrographs and elemental composition of the samples were obtained using a field emission scanning electron microscope (Zeiss Auriga 60) equipped with an energy-dispersive X-ray spectrometer (Oxford X-Max). For energy-dispersive X-ray (EDX) analysis, technical catalysts in their reduced form were crushed and fixed over a holder using carbon tape. The chemical composition is expressed as the average of five measurements on individual particles for each powder sample. For EDX mapping, the technical catalysts were cold-drawn in epoxy resin and left to cure for 24 h. The specimens were then polished to obtain the cross-section of the spheres and coated by gold sputtering.

X-ray diffraction (XRD) patterns were collected within the 2θ range 20−80° in a Bruker type XRD D8 Advance A25 diffractometer using a Cu Kα radiation (λ = 1.5406 Å), a voltage of 40 kV, a current of 40 mA, and a step size of 0.02° (with 2 s duration at each step).

https://doi.org/10.1021/acsaenm.2c00214
ACS Appl. Eng. Mater. 2023, 1, 1106−1115

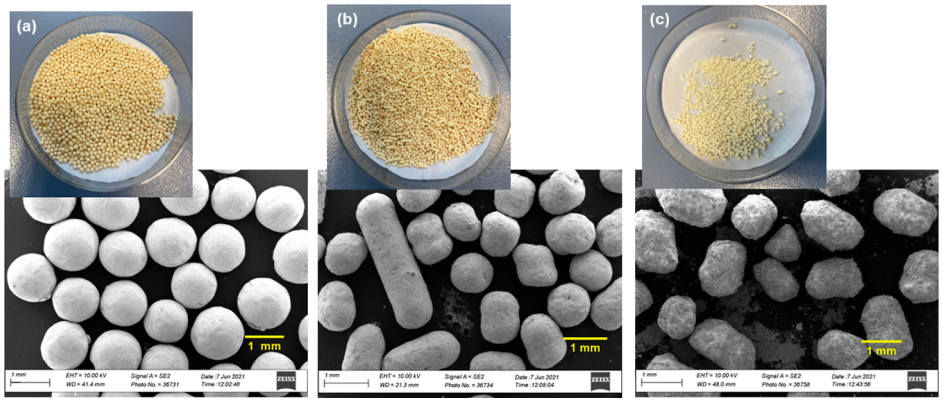

Figure 1. SEM images of (a) CeO_2-MC, (b) CeO_2-HEC, and (c) CeO_2-PVP after calcination at 500 °C. Scalebar is 1 mm.

The average crystal sizes of Ni^0 and CeO_2 were estimated using the Scherrer's equation at $2\theta = 44.50°$ for Ni(111) and $2\theta = 47.36°$ for CeO_2 (220): $D = (K\lambda/\beta\cos\theta)$, where λ is the X-ray wavelength, β is the full width of the diffraction line at half-maximum (FWHM), and θ is the Bragg angle.

The viscosity of the plasticizers was measured in a Brookfield viscometer DV2T at 24 °C. The concentration of the plasticizer solutions was 2% in water (w/v).

N_2-physisorption measurements were conducted in the TriStar II 3020-Micrometrics analyzer at liquid nitrogen temperature. Prior to the measurements, the samples were degassed at 90 °C for 1 h and then at 250 °C overnight in a FlowPrep 060-Micromeritics. The Brunauer–Emmett–Teller (BET) method was applied to calculate the BET surface area for a relative pressure (P/P_0) range of 0.05–0.3. The average pore size was determined by applying the Barrett–Joyner–Halenda (BJH) method to the desorption branch of the isotherms. The total pore volume was determined from the maximum adsorption value at $P/P_0 = 0.997$.

Temperature-programed reduction (H_2-TPR) measurements were conducted in an AutoChem (Micromeritics) instrument using 12 vol % H_2/Ar at a flow of 50 N mL·min^{-1} in the temperature range of 35–800 °C at a heating ramp of 10 °C·min^{-1}. The amount of H_2 uptake was measured with a thermal conductivity detector. 100 mg of sample were used for each measurement. The metallic surface area was determined by pulsed CO chemisorption in an AutoChem (Micromeritics) instrument. Prior to adsorption measurements, samples were reduced in H_2 flow at 350 (Ni–CeO_2) and 500 °C (Ni–Al_2O_3 and Ni–CeO_2–Al_2O_3) for 3 h.

The skeletal density has been measured with a Quantachrome Ultrapyc 1200e Automatic Density Analyzer. The bulk density (ρ_{bulk}) has been estimated considering the mass of pellets that fill a cylinder of a capacity 0.5 mL.

The ultimate compression strength of the materials was determined in a Zwick-Roell universal testing machine with a load cell of 200 N. The results are given as the average of ten measures.

2.3. Catalytic Activity

Catalytic tests were performed in a fixed-bed catalytic reactor with 13 mm of internal diameter and 305 mm of length (Microactivity Reference, PID Eng&Tech). 0.3 g of dry catalyst pellets were used for each experiment. The catalyst was diluted with 3 g of Al_2O_3 spheres (Norpro Saint Gobain) of $d_p = 1$ mm to ensure isothermal behavior through the catalyst bed. A K-type thermocouple was placed in the middle of the diluted catalyst bed to monitor the temperature of the reaction. Before the experiments, catalysts were reduced in situ under a H_2 flow (100 N mL·min^{-1}) at 350 °C (CeO_2-supported) and 500 °C (Al_2O_3-supported) for 3 h (ramp 5 °C·min^{-1}), then cooled to 50 °C with the same ramp. Experiments were conducted using a H_2/CO_2 stoichiometric molar ratio of 4.0 (Linde), a pressure of 5.0 bar·g and a gas flow $F = 100–200$ mL·min^{-1}. Catalyst screening was performed isothermally at intervals of 50 °C in the temperature range of 250–350 °C, starting from the lowest temperature and waiting until steady state was attained. After reaction, the products passed through a cold liquid–gas separator (5 °C), where water was trapped, and the dry flow was measured by means of a mass flow meter (MF, Bronkhorst). The composition of the dry gas was determined with an on-line gas micro-chromatograph (490 microGC, Agilent Technologies) calibrated for CH_4, H_2, CO, CO_2, C_2H_4, and C_2H_6 and automatically analyzed every 2.5 min along the screening experiments and hourly during the stability test. Three measures were taken at each temperature, and the results have a relative error of the 2%. Stability experiments were conducted at a fixed temperature of 300 °C, a pressure of 5 bar·g and $F = 200$ N mL·min^{-1}. The CO_2 conversion (χCO_2) was calculated following eq 1, where Fco_2 represents the molar flow rate of CO_2 in the inlet and outlet gas. The selectivity toward CH_4 was calculated following eq 2.

$$\chi_{CO_2} = \left(1 - \frac{F_{CO_2,out}}{F_{CO_2,in}}\right) \quad (1)$$

$$S_{CH_4} = \frac{F_{CH_4,out}}{F_{CH_4,out} + F_{CO,out} + F_{C_2C_6,out} + F_{C_2C_4,out}} \quad (2)$$

The activity of the catalysts was calculated through eq 3

$$\text{activity} = \frac{\chi_{CO_2 t}}{\chi_{CO_2 0}} \quad (3)$$

where $\chi_{CO_2 t}$ is the CO_2 conversion at time t and $\chi_{CO_2 0}$ is the CO_2 conversion at 0 h.

Gas hourly space velocity (GHSV) was calculated as the ratio of the inlet flow rate in standard conditions to the volume of the catalyst (eq 4). The volumetric flow rate (F) was adjusted from 200 to 90 N mL·min^{-1}, whereas the catalyst mass was kept constant ($m_{cat} = 0.3$ g). The bulk densities (ρ_{bulk}) of the catalysts are gathered in Table S1.

$$\text{GHSV} = \frac{F}{\frac{m_{cat}}{\rho_{bulk}}} \quad (4)$$

Diffuse reflectance infrared Fourier transform spectroscopy (DRIFTS) measurements were performed on a Bruker-Vertex70 spectrophotometer equipped with a MCT detector and a high-temperature reaction cell (Harrick Praying Mantis) with two ZnSe windows. Prior to the experiments, the samples were reduced at 350 °C in the reaction cell under an Ar/H_2 flux. A flux of 20 N mL·min^{-1} was applied for the CO_2 methanation reaction with an Ar/H_2/CO_2 ratio of 15:4:1. The reaction was studied in the temperature range of 100–350 °C, at intervals of 50 °C. Background spectra were recorded under Ar at each temperature.

https://doi.org/10.1021/acsaenm.2c00214
ACS Appl. Eng. Mater. 2023, 1, 1106–1115

3. RESULTS AND DISCUSSION

3.1. Physicochemical Properties of the Shaped Catalyst Carriers

Attempts to fabricate CeO_2 pellets in the absence of an extrusion-aid agent were unsuccessful and led to migration of the liquid phase out of the die holes, leaving the solid residue inside the extruder unit, a behavior that is often attributed to a heterogeneous particle size distribution or instability of the dispersion. In an attempt to improve the flow properties of the CeO_2 powders, the use of MC, HEC, and PVP as extrusion-aid agents was evaluated at an equal CeO_2/extrusion-aid agent ratio (10:0.55) and applying the same manufacturing conditions. After optimization of the water content in each paste, the three plasticizers allowed to obtain CeO_2-based extrudates, despite displaying very different viscosity properties (see Figure S1). The extrusion was followed by spheronization and thermal treatment to achieve the technical support.

SEM was used to evaluate the morphologies of the CeO_2 pellets fabricated using MC, HEC, and PVP, denoted as CeO_2-MC, CeO_2-HEC, and CeO_2-PVP, respectively. Figure 1 shows that the CeO_2-MC pellets presented a spherical form with mean diameters centered at 1.3 ± 0.3 mm and exhibited smooth surfaces. In the same conditions, when HEC was used as plasticizer, mostly dumb-bell shaped pellets and rods of variable sizes were obtained. While in the case of CeO_2-MC, rounding was achieved, when using HEC, no spherical shapes were attained even after increasing the spheronization time.[47] The high degree of entanglement of HEC and the ability to form hydrogen bonds with the Ce−OH and Ce−OH_2^+ surface groups through diverse moieties (hydroxyl, ether, and hydroxyethyl groups) presumably result in a high cohesive strength that prevented the pellets from further breaking.

The CeO_2-PVP structures were very irregular and heterogeneous, and a high fraction of powder was observed in the spheronizer plate, detached from the main bodies. Despite facilitating the extrusion of the CeO_2-based paste, PVP exhibited too weak interaction with the CeO_2 particles, resulting in a very high attrition of the materials during the spheronization process. From these results, it is inferred that the use of plasticizers is mandatory for the extrusion of the CeO_2 powders. Besides, as observed in this experimental study, the nature of the plasticizer plays a determinant role in the morphology of the CeO_2 catalyst carrier manufactured by extrusion-spheronization.

The main structural and surface characteristics of the shaped CeO_2 carriers are summarized in Table 1. As a reference, the data of the CeO_2 powder obtained by calcination of cerium nitrate is also included. BET surface areas (SA_{BET}) of CeO_2-MC, CeO_2-HEC, and CeO_2-PVP pellets were 60.3, 59.3, and 58.4 $m^2 \cdot g^{-1}$, respectively, close to the original value of 61.9 $m^2 \cdot g^{-1}$ of the CeO_2 powder. All isotherms correspond to a type IV (Figure S2), characteristic of mesoporous materials.[48] To study how the pellet calcination step affected the porosity of the CeO_2 used, a sample of CeO_2 powder was subjected to the same thermal treatment as the green pellets (500 °C, 4 h, 5 °C/min) and used as a blank, henceforth referred to as CeO_2p-t. A decrease in SA_{BET} was observed in the thermally treated CeO_2 powder sample, 57.3 $m^2 \cdot g^{-1}$ (Table S2) while in the mesopore range (Figure S3), no significant variations were detected. This loss of surface area is therefore attributed to the collapse of smaller pores caused by the increase in contact areas between the CeO_2 grains induced by temperature. Figure 2 shows the mesopore size distribution of the calcined CeO_2 pellets. The generation of additional mesoporosity resulting from the burnout of the organic plasticizers is evidenced by the shift toward smaller pore sizes observed for the three CeO_2 pellets that is neither present in the CeO_2p-t sample nor in the original CeO_2 powder. The generation of these new mesopores during the calcination step is reflected by the milder decrease in SA_{BET} values of CeO_2-MC, CeO_2-HEC, and CeO_2-PVP in comparison to that of the thermally treated CeO_2 powder used as a blank.

Commercial Al_2O_3 spheres have a mean diameter of 1.1 ± 0.1 mm and a spherical shape. N_2-physisorption measurements revealed a surface area of 203.1 $m^2 \cdot g^{-1}$ and a pore volume of 0.67 $cm^3 \cdot g^{-1}$, considerably higher values than their CeO_2 counterparts (Figure S4).

The mechanical properties of the materials were evaluated before and after thermal processing by means of a mechanical rupture test (see Table S3). Green bodies exhibited higher mechanical resistances, conferred by the plasticizer, with a remarkable value of 26 N for the CeO_2-HEC. This higher resistance of CeO_2-HEC pellets could however be explained by the higher section of the material, given its dumb-bell geometry. After calcination of the pellets and removal of the organic additives, their mechanical strength dropped to 2−5 N, a considerably weaker resistance to compression with respect to commercial Al_2O_3.

A very relevant difference between CeO_2- and Al_2O_3-based carriers is their skeletal density. The tabulated density of bulk ceria is almost two times that of alumina,[49] which is maintained in the shaped carriers. As it will be discussed below, carrier density has important implications on the amount of catalyst that can be loaded into a given device, and therefore, in the cost-effectiveness of the operation.

Among the plasticizers evaluated in this study, MC provided adequate rheological properties of the CeO_2-based paste and cohesion of the powders in the green bodies, resulting in well-defined spherical shapes, smooth surfaces, and reproducible results in terms of shape and morphology of the obtained structures. CeO_2-MC spheres were thus selected to continue with this study.

Table 1. Physical Properties of CeO_2 Powder, CeO_2-Based Pellets, and Al_2O_3 Pellets

sample	SA_{BET} ($m^2 \cdot g^{-1}$)	pore volume ($cm^3 \cdot g^{-1}$)	pore diameter (nm)	skeletal density ($g \cdot cm^{-3}$)
CeO_2 powder	61.9	0.20	12.6	
CeO_2-MC	60.3	0.19	11.9	6.1
CeO_2-HEC	59.3	0.18	11.0	6.0
CeO_2-PVP	58.4	0.17	10.7	6.1
Al_2O_3	203.1	0.67	10.2	3.1

3.2. Catalyst Characterization

CeO_2-MC and Al_2O_3 carriers were further impregnated with Ni, hereinafter referred to as Ni−CeO_2 and Ni−Al_2O_3, whereas Ni−CeO_2−Al_2O_3 was prepared by co-impregnation of Ni and Ce species on Al_2O_3 spheres. This approach allows comparing the use of ceria as a promoter into commercial supports or its use directly as a bulk support.

The composition of the samples and their textural properties are shown in Table 2. Elemental compositions obtained from

https://doi.org/10.1021/acsaenm.2c00214
ACS Appl. Eng. Mater. 2023, 1, 1106−1115

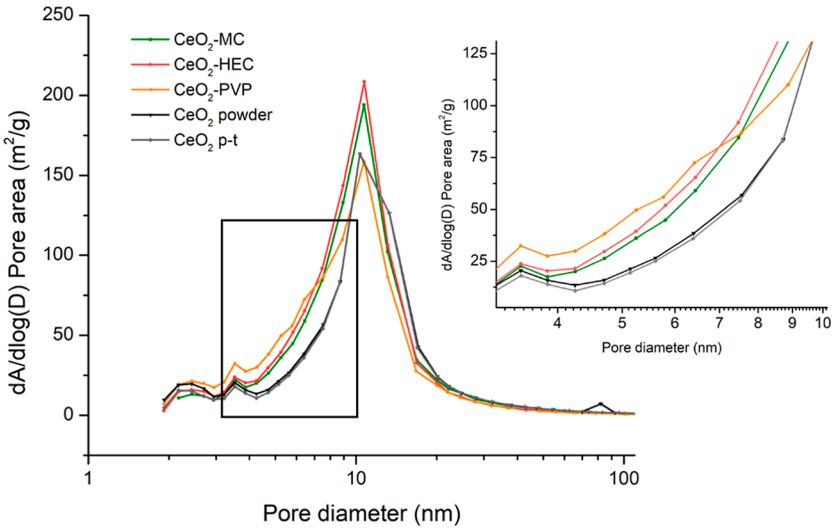

Figure 2. BJH Desorption dA/dlog(D) Pore area as a function of pore diameter for the CeO_2 powder, CeO_2p-t, and CeO_2 pellets.

Table 2. Properties of the Ni−CeO_2, Ni−CeO_2−Al_2O_3, and Ni−Al_2O_3 Catalysts

catalyst	Ni (wt %)	CeO_2 (wt %)	SA_{BET} ($m^2 \cdot g^{-1}$)	pore volume ($cm^3 \cdot g^{-1}$)	pore diameter (nm)	Ni size (nm)	CeO_2 size (nm)	metallic surface area ($m^2 \cdot g^{-1}$)
Ni−CeO_2	10.1 ± 0.2		46.3	0.16	12.3	22.0	11.5	0.40
Ni−CeO_2−Al_2O_3	9.7 ± 0.4	10.5 ± 0.3	152.2	0.49	10.1		5.8	0.78
Ni−Al_2O_3	9.6 ± 0.4		172.7	0.58	10.7			1.17

EDX analysis were very close to the nominal ones. The cross-section of the catalysts was analyzed by SEM−EDX, which evidenced an even distribution of the Ni and Ce species within the support structure (see Figures S5−S7). On the other hand, the surface area of the CeO_2-based carriers was reduced by a 23% by the incorporation of Ni and in Al_2O_3-based carriers by a 15% and a 26%, in agreement with the incorporation of Ni, and Ni and Ce species, respectively (Figure S8). All catalysts display similar pore diameter, in the mesorange.

The reducibility of the catalysts was studied by H_2-TPR measurements, see Figure 3. The H_2 uptake curve of the non-reduced Ni−CeO_2 catalyst displayed two peaks below 250 °C, assigned to the reduction of surface oxygen species,[50] and a big peak centered at 290 °C attributed to the reduction of relatively free NiO, weakly interacting with the CeO_2 surface. Reduction of bulk CeO_2 was only observed below 700 °C.[51] The interaction of NiO with Al_2O_3 supports is stronger; in this aspect, reduction of the Ni−Al_2O_3 begins at higher temperatures. NiO species were identified as mildly (400−580 °C) and strongly interacting (600−750 °C) with the Al_2O_3 support.[52] A small fraction reducing above 700 °C is attributed to the reduction of NiO in a nickel aluminate phase. The influence of CeO_2 when reducing the Ni−CeO_2−Al_2O_3 catalyst is evidenced by the H_2 uptake peak observed between 330 and 420 °C, yet it only represents 18% of the NiO in the sample, and the main reduction of NiO starts above 400 °C.

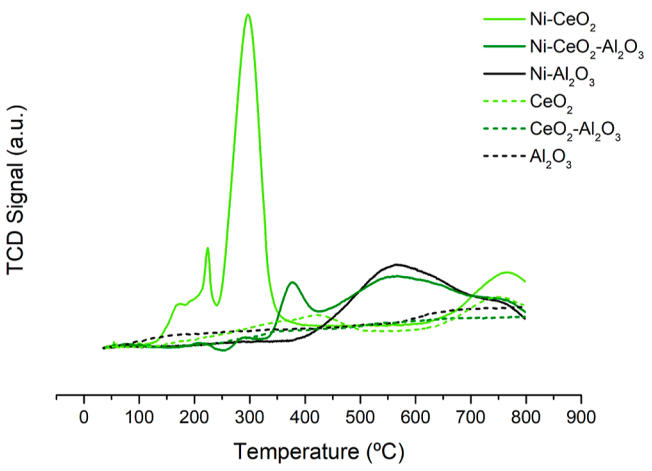

Figure 3. H_2-TPR profiles of Ni−CeO_2, Ni−CeO_2−Al_2O_3, and Ni−Al_2O_3 catalysts. Dashed lines: H_2-TPR profiles of non-impregnated CeO_2, CeO_2−Al_2O_3, and Al_2O_3 supports.

Barrault et al.[53] already reported the influence of CeO_2 and Al_2O_3 supports on the reducibility of NiO species. Here, while in Ni−CeO_2, total reduction was achieved before 400 °C, in Ni−Al_2O_3, the bulk of the process took place between 400 and 700 °C. The possibility to reduce the catalyst at mild temperatures arises as a technological advantage of the CeO_2-based carriers with respect to the Al_2O_3 ones, as most commercial reactors are incapable of heating the hydrogen gas above 325−450 °C.[54] In this regard, energy efforts during the reduction protocol are substantially lower when using CeO_2-based catalyst carriers.

Figure 4 shows the XRD diffractograms of the reduced catalysts. In the XRD profile of the Ni−CeO_2 catalyst, only the typical diffractions of metallic Ni were observed, and those corresponding to the NiO phase were not detected, which points to a complete reduction of the catalyst at the chosen temperature of 350 °C. The crystallite size of Ni particles was estimated by the Scherrer's equation using the peak at 2θ = 44.5°, and it was found to be 22.0 nm. The same way, a size of 11.5 nm was estimated for the CeO_2 phase using the peak at 2θ = 28.6°. In Ni−CeO_2−Al_2O_3 and Ni−Al_2O_3 diffractograms,

https://doi.org/10.1021/acsaenm.2c00214
ACS Appl. Eng. Mater. 2023, 1, 1106−1115

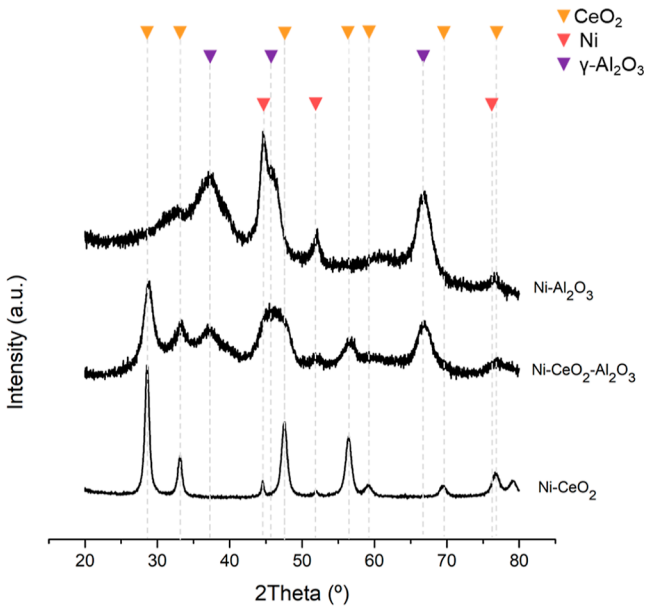

Figure 4. XRD spectra of (a) Ni−CeO_2, (b) Ni−CeO_2−Al_2O_3, and (c) Ni−Al_2O_3 catalysts.

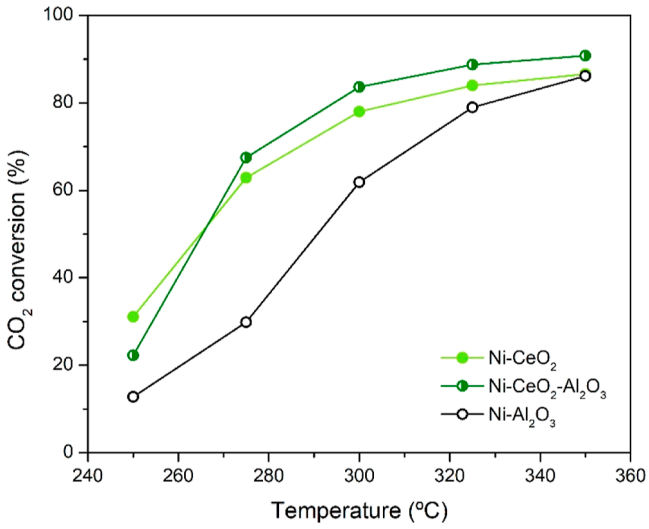

Figure 5. CO_2 conversion (%) of Ni−CeO_2, Ni−CeO_2−Al_2O_3, and Ni−Al_2O_3 catalysts as a function of reaction temperature at constant flow F = 200 NmL·min^{-1}. P = 5 bar·g, m_{cat} = 0.3 g, and H_2/CO_2 molar ratio = 4.

reduced at 500 °C, broad peaks matching those of Ni^0 were also visible. The Scherrer's equation for Ni crystals was not applied in these cases as broad peaks of γ-Al_2O_3 are overlapped. A qualitative comparison of the Ni^0 peaks suggests that Ni crystals are smaller in Ni−CeO_2−Al_2O_3 and Ni−Al_2O_3 than in their CeO_2-based counterparts, which can be directly related to the lower porosity of CeO_2-based carriers. The crystallite size of the CeO_2 phase in Ni−CeO_2−Al_2O_3 was estimated at 5.8 nm. The co-impregnation of CeO_2 on the Al_2O_3 support resulted in a smaller particle size compared to that of the CeO_2 powder used as support in Ni−CeO_2.

CO-chemisorption analysis of the reduced Ni−CeO_2 catalyst revealed a metallic surface area of 0.40 $m^2 \cdot g^{-1}$, whereas those obtained for Ni−CeO_2−Al_2O_3 and Ni−Al_2O_3 were 0.78 and 1.17 $m^2 \cdot g^{-1}$, respectively. The higher specific surface area and total pore volume of Al_2O_3 spheres compared to those of CeO_2 allowed for a better accommodation and dispersion of Ni species over the surface of the support. The identification of well-dispersed nickel species is well aligned with the presence of small NiO particles strongly interacting with the Al_2O_3 support, identified by the H_2-TPR measurements.[55,56] As a whole, physico-chemical characterization of shaped catalysts showed that Al_2O_3 (doped or not by CeO_2) presented larger porosity, more Ni active sites and higher Ni dispersion than its CeO_2 counterparts.

3.3. Catalytic Activity in CO_2 Methanation

The relevance of these novel carriers was evaluated, as a proof-of-concept, in the CO_2 methanation reaction. The catalytic performance of Ni−CeO_2, reduced at 350 °C, and Ni−CeO_2−Al_2O_3 and Ni−Al_2O_3 catalysts, reduced at 500 °C, was analyzed in the temperature range of 250−350 °C at 5 bar·g and a constant volume flow of 200 N mL·min^{-1}. For the Ni−CeO_2 catalyst, selectivity to CH_4 was in all cases ≥99%, whereas lower values were obtained for the Ni−CeO_2−Al_2O_3, ≥97%, and the Ni−Al_2O_3 catalysts, ≥85% (see Tables S4−S9).

Ni−CeO_2−Al_2O_3 exhibited moderately higher conversions, as shown in Figure 5. In these circumstances, despite having three times the surface area and twice the metallic surface of its CeO_2 counterpart, the CeO_2-promoted catalyst was only slightly more active. The higher activity of Ni−CeO_2−Al_2O_3 over Ni−CeO_2 is thus due to the higher degree of dispersion of the active metal centers. The promoter effect of CeO_2 is confirmed by the higher conversions of Ni−CeO_2−Al_2O_3 with respect to the Ni−Al_2O_3 analogue, even with lower metal surface areas. Turnover frequencies (TOF) were calculated based on the CO chemisorption results and considering a CO/Ni adsorption stoichiometry of 1:1 (see Table S10). At a reaction temperature of 300 °C, the TOF values exhibited by Ni−CeO_2 were 27.4 mol $CH_4 \cdot min^{-1} \cdot mol^{-1}$ Ni, higher than the 22.7 and 12.2 mol $CH_4 \cdot min^{-1} \cdot mol^{-1}$ Ni achieved by Ni−CeO_2−Al_2O_3 and Ni−Al_2O_3, respectively. These values evidence that the greater CO_2 conversions obtained by Ni−CeO_2−Al_2O_3 account for the higher surface area of the Al_2O_3 support, which enables better dispersion of the active phase.

Taking into consideration that gas hourly space velocity (GHSV) is a key parameter to validate the performance of the catalysts in microchannel fixed-bed reactors,[54] Figure 6 compares the activity of the three catalysts working at the same GHSV. In this case, the Ni−CeO_2 catalyst showed an outstanding performance compared to the commercial Al_2O_3 spheres, especially at lower temperatures. In the evaluated temperature range of 250−350 °C, the Ni−CeO_2 achieved CO_2 conversions between 69 and 95% when reduced at 350 °C. In most industrial processes, catalyst is loaded in a given reactor volume; and very especially, in advanced microreactors which aim at process intensification.[57−59] Accordingly, the implementation of the shaped CeO_2-based catalysts arises as a powerful alternative to the conventional Al_2O_3-based ones since, at a given reactor volume, (i) higher CH_4 yields are obtained, (ii) reaction takes place at lower temperatures, and (iii) catalyst can be in situ reduced at milder conditions. The good performance of the CeO_2-based supports in the methanation of CO_2 suggests that their application can be broadened to other reactions of industrial interest in which CeO_2 is commonly used as a reaction promoter, like the Fischer−Tropsch synthesis or the reforming of methane.

Eventually, the stability of the Ni−CeO_2 catalyst was evaluated for 40 h at 5 bar·g and using a reaction temperature

https://doi.org/10.1021/acsaenm.2c00214
ACS Appl. Eng. Mater. 2023, 1, 1106−1115

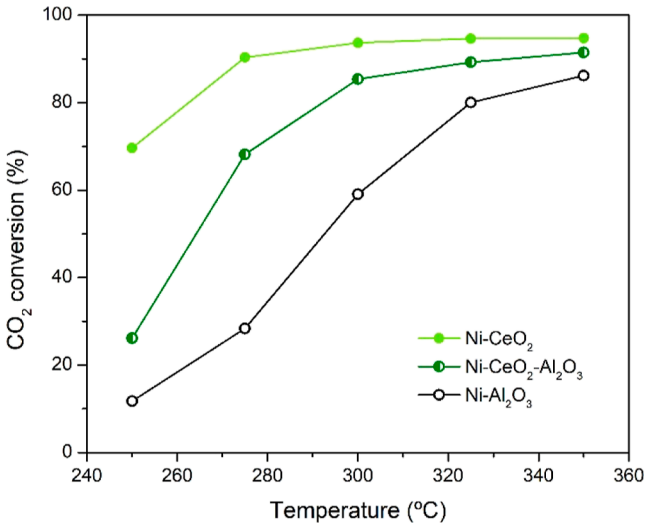

Figure 6. CO_2 conversion (%) of Ni−CeO_2, Ni−CeO_2−Al_2O_3, and Ni−Al_2O_3 catalysts as a function of reaction temperature at constant GHSV = 27,200 h^{-1}. Reaction conditions: P = 5 bar·g, m_{cat} = 0.3 g, and H_2/CO_2 molar ratio = 4.

of 300 °C. Figure 7 shows the evolution of the catalytic activity over the course of this long-term experiment. At the selected

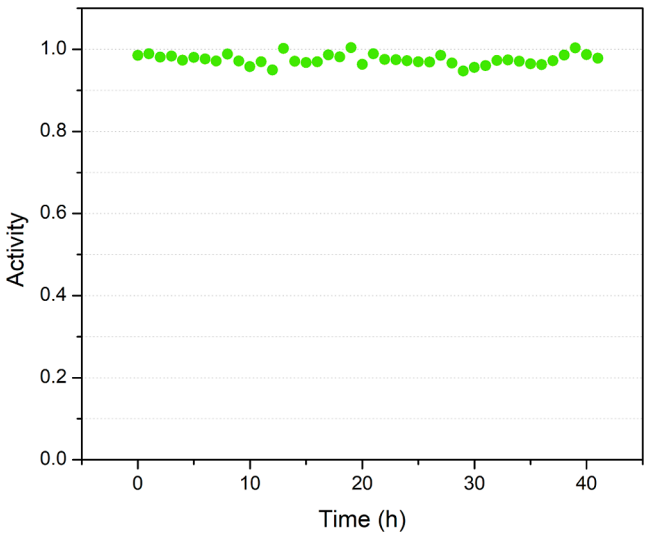

Figure 7. Relative CO_2 conversion of Ni−CeO_2 over a 40 h reaction at 300 °C.

reaction conditions, no activity loss was observed as catalytic activity was kept very close to 1.

In order to understand the higher catalytic activity of CeO_2 catalyst pellets, despite presenting inferior physico-chemical properties in terms of porosity, Ni dispersion, and metal size; the species formed on the surface of the Ni−CeO_2 and Ni−CeO_2−Al_2O_3 catalysts during the methanation reaction were studied by in situ DRIFTS experiments at different temperatures. For simplification purposes, the intense band corresponding to gaseous CO_2 appearing at 2350 cm^{-1} has been hidden from the spectra. In accordance with the catalytic tests, in the Ni−CeO_2 spectra, Figure 8a, the characteristic vibrations of gas-phase CH_4 (3015 and 1304 cm^{-1}) can be detected at very low temperatures and grow above 200 °C. At high temperatures, bands at 1440 cm^{-1} and 1340 cm^{-1} matching those of hydrogen carbonate (HCO_3^-) and monodentate carbonate (m-CO_3^{2-}) species can also be detected. The broad band around 3400 cm^{-1} and the peak at 1625 cm^{-1}, whose presence becomes evident at higher temperatures, are attributed to the H_2O product of the methanation reaction.[60] To shed some light on the interaction between CO_2 and the CeO_2 support, DRIFTS experiments were recorded on bare CeO_2-MC spheres when exposed to the same conditions (see Figure S9). In contrast to the spectra recorded for the Ni−CeO_2 catalyst, where almost no surface species are observed, the adsorption of bicarbonates at low temperatures can be identified on the surface of the CeO_2-MC support, followed by the progressive formation of HCO_3^-, m-CO_3^{2-}, and formates ($HCOO^-$) at higher temperatures. Interestingly, no methanation is observed in the absence of nickel. Such lack of bands in the 1800−1000 cm^{-1} range for the Ni−CeO_2 catalyst could indicate (a) that the CeO_2 surface sites are hindered by the impregnated Ni species or (b) a high rate of formation and depletion of the reaction intermediates in the presence of Ni.

A very different interaction with the substrates was observed for the Ni−CeO_2−Al_2O_3 catalyst, as shown in Figure 8b. In comparison to its Ni−CeO_2 counterpart, the formation of methane was detected at higher temperatures, namely 250 °C, thus confirming the lower activity of this catalyst at temperatures below 300 °C. Up to 150 °C, the bands at 3622, 1650, 1437, and 1228 cm^{-1} suggest the adsorption of HCO_3^-[61,62] as the only surface species. The formation of $HCOO^-$ when increasing temperature is evidenced by the bands at 2990, 1590, and 1374 cm^{-1} gradually appearing from 200 °C up. The presence of formates as the major species at the surface simultaneous to the generation of methane suggests that formates are the reaction intermediate for the Ni−CeO_2−Al_2O_3 catalyst, as proposed by Cárdenas-Arenas et al. for a Ni−Al_2O_3 system.[63]

In this respect, the contribution of CeO_2 as a promoter was not detected, although large amounts of CeO_2 were introduced in the Ni−CeO_2−Al_2O_3 catalyst. DRIFTS experiments confirmed that when the novel CeO_2-based catalyst was used, methanation took place at lower reaction temperatures than for the CeO_2-promoted Al_2O_3 counterpart, proving the suitability of the developed support for this reaction.

The significance of the Ni−CeO_2 catalyst becomes evident in novel reactor technologies such as small-size reactors that operate by free convection, where the temperature profile varies throughout the reactor.[64,65] The implementation of the Ni−CeO_2 catalyst at the low temperature reactor zone seems a good strategy to overcome the kinetic limitations of commercial Al_2O_3-based catalysts, thus enhancing the reaction rate and the efficiency of the whole reactor. The novel catalyst showed significantly higher CO_2 conversions, especially at lower temperatures, achieving conversions between 69 and 95% in the evaluated temperature range of 250−350 °C when reduced at 350 °C. On the other hand, the conventional Al_2O_3-based catalyst showed lower CO_2 conversions, ranging from 11 to 91% in the same temperature range when reduced at 500 °C. The difference in thermal conductivity of the support materials (35 $W·m^{-1}·K^{-1}$ for bulk γ-Al_2O_3 versus 7−12 $W·m^{-1}·K^{-1}$ for CeO_2[66,67]) must however be considered when implemented in industrial reactors and is a critical parameter in the reactor design step. In the case of the methanation reaction, the thermal properties of CeO_2 supports can become

https://doi.org/10.1021/acsaenm.2c00214
ACS Appl. Eng. Mater. 2023, 1, 1106−1115

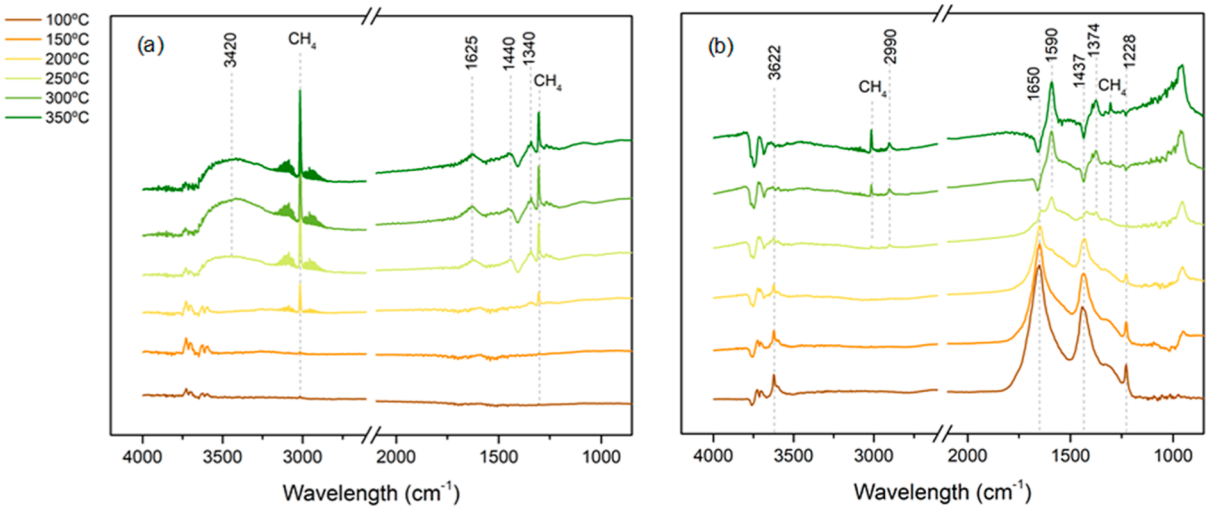

Figure 8. In situ DRIFTS spectra of the methanation of CO_2 over (a) Ni−CeO_2 and (b) Ni−CeO_2−Al_2O_3 catalysts reduced at 350 °C.

an asset when applied in the low temperature zone of reactors that operate in polytropic conditions.

The application of shaped CeO_2-based catalysts in industrial processes, especially in advanced microreactors which aim at process intensification, offers a novel alternative to traditional commercial Al_2O_3-based supports. At a given reactor volume, the shaped CeO_2-based catalysts exhibit higher CH_4 yields, operate at lower temperatures, and can be in situ reduced at milder conditions. Therefore, the results obtained in this study have significant implications for the development of more efficient catalytic systems for CO_2 methanation. The hybrid nature of the manuscript, combining both general catalyst characterization, in situ DRIFTS, catalytic tests, and the development of a new catalyst, provides a comprehensive understanding of the catalyst's performance and can serve as a valuable reference for researchers and engineers working in the field of CO_2 methanation.

4. CONCLUSIONS

A novel manufacturing process to fabricate mm-sized mesoporous CeO_2-based catalyst carriers was established. Mesoporous CeO_2 powders were prepared by calcination, ball milled, mixed with an appropriate plasticizer and water under mild acidic conditions, homogenized, extruded, shaped in spherical form, and finally calcined. From this work, it was determined that the use of a plasticizer was necessary for the shaping process and that, among the plasticizers studied, MC provided well-defined spherical shapes and reproducible batches. The so-obtained CeO_2-based carriers were evaluated in the catalytic methanation of CO_2 by the incorporation of Ni as the active phase and compared to the use of CeO_2 as a promoter on commercial Al_2O_3 supports. CeO_2 catalyst carriers showed outstanding performance at equal reactor volume, and importantly, using a moderate reduction protocol. The activity of the CeO_2 pellets as catalytic supports is however constrained by the lower surface areas of CeO_2 regarding that of Al_2O_3-based materials. This point, as well as the mechanical resistance of the materials, has to be addressed in the eventual commercialization phase of the product. The high activities observed were attributed to the better reducibility of Ni over the CeO_2 spheres and the different reaction mechanism that allowed activating the production of CH_4 at lower temperatures. On account of the results obtained, the CeO_2 spheres fabricated in this study appear as promising materials for application in emerging reactor technologies such as advanced compact reactors and free-convection devices, in which the activity of commercial Al_2O_3-based catalysts is limited by catalyst volume and the high temperatures required for their activation. The activity of these new materials is not restricted to the methanation of CO_2 and their application can be extended to reactions like Fischer−Tropsch, the synthesis of methanol, or methane reforming by impregnation of the appropriate active phase.

■ ASSOCIATED CONTENT

Supporting Information

The Supporting Information is available free of charge at https://pubs.acs.org/doi/10.1021/acsaenm.2c00214.

Bulk density of the catalysts, viscosity of plasticizers, N_2-physisorption isotherms, mechanical rupture tests, EDX elemental mapping of the catalysts cross-sections, TOF values of the catalysts in the CO_2 methanation reaction, and DRIFTS spectrum of the methanation of CO_2 over a bare CeO_2 support (PDF)

■ AUTHOR INFORMATION

Corresponding Author

Elena Martín Morales − *Catalonia Institute for Energy Research (IREC), 08930 Sant Adrià de Besòs, Spain;* orcid.org/0000-0002-1363-7946; Email: emartin@irec.cat

Authors

Andreína Alarcón − *Catalonia Institute for Energy Research (IREC), 08930 Sant Adrià de Besòs, Spain; Escuela Superior Politécnica del Litoral, ESPOL, Facultad de Ingeniería en Ciencias de la Tierra, 090101 Guayaquil, Ecuador*

Martí Biset-Peiró − *Catalonia Institute for Energy Research (IREC), 08930 Sant Adrià de Besòs, Spain;* orcid.org/0000-0002-1255-7733

Elena Xuriguera − *Facultat de Química, Universitat de Barcelona, 08028 Barcelona, Spain*

Jordi Guilera − *Catalonia Institute for Energy Research (IREC), 08930 Sant Adrià de Besòs, Spain; Facultat de*

https://doi.org/10.1021/acsaenm.2c00214
ACS Appl. Eng. Mater. 2023, 1, 1106−1115

Química, Universitat de Barcelona, 08028 Barcelona, Spain; orcid.org/0000-0002-7184-6404

Complete contact information is available at: https://pubs.acs.org/10.1021/acsaenm.2c00214

Notes

The authors declare no competing financial interest.

■ ACKNOWLEDGMENTS

This work was financed by the project TED2021-132365B-I00, funded by MCIN/AEI/10.13039/501100011033 and by the European Union "NextGenerationEU"/PRTR. The authors also acknowledge the financial support of the project 2019PROD00091, co-financed by the European Union through the European Regional Development Fund (ERDF) and supported by the University and Research Secretary of the Business Department and Knowledge of the Generalitat de Catalunya. Authors kindly thank Dr. Albert Llorente for the assistance in the characterization of materials.

■ REFERENCES

(1) Trovarelli, A.; Deleitenburg, C.; Dolcetti, G.; Lorca, J. L. CO_2 Methanation Under Transient and Steady-State Conditions over Rh/CeO_2 and CeO_2-Promoted Rh/SiO_2: The Role of Surface and Bulk Ceria. *J. Catal.* **1995**, *151*, 111−124.

(2) Montini, T.; Melchionna, M.; Monai, M.; Fornasiero, P. Fundamentals and Catalytic Applications of CeO_2-Based Materials. *Chem. Rev.* **2016**, *116*, 5987−6041.

(3) Mullins, D. R. The Surface Chemistry of Cerium Oxide. *Surf. Sci. Rep.* **2015**, *70*, 42−85.

(4) Martínez-Arias, A.; Gamarra, D.; Fernández-García, M.; Hornés, A.; Bera, P.; Koppány, Z.; Schay, Z. Redox-Catalytic Correlations in Oxidised Copper-Ceria CO-PROX Catalysts. *Catal. Today* **2009**, *143*, 211−217.

(5) Furler, P.; Scheffe, J. R.; Steinfeld, A. Syngas Production by Simultaneous Splitting of H_2O and CO_2 via Ceria Redox Reactions in a High-Temperature Solar Reactor. *Energy Env. Sci* **2012**, *5*, 6098−6103.

(6) Trovarelli, A.; Llorca, J. Ceria Catalysts at Nanoscale: How Do Crystal Shapes Shape Catalysis? *ACS Catal.* **2017**, *7*, 4716−4735.

(7) Bunluesin, T.; Gorte, R. J.; Graham, G. W. Studies of the Water-Gas-Shift Reaction on Ceria-Supported Pt, Pd, and Rh: Implications for Oxygen-Storage Properties. *Appl. Catal. B Environ.* **1998**, *15*, 107−114.

(8) Colussi, S.; Gayen, A.; Farnesi Camellone, M.; Boaro, M.; Llorca, J.; Fabris, S.; Trovarelli, A. Nanofaceted Pd-O Sites in Pd-Ce Surface Superstructures: Enhanced Activity in Catalytic Combustion of Methane. *Angew. Chem., Int. Ed.* **2009**, *48*, 8481−8484.

(9) Lucentini, I.; Casanovas, A.; Llorca, J. Catalytic Ammonia Decomposition for Hydrogen Production on Ni, Ru and Ni Ru Supported on CeO_2. *Int. J. Hydrog. Energy* **2019**, *44*, 12693−12707.

(10) Adijanto, L.; Sampath, A.; Yu, A. S.; Cargnello, M.; Fornasiero, P.; Gorte, R. J.; Vohs, J. M. Synthesis and Stability of Pd@CeO_2 Core−Shell Catalyst Films in Solid Oxide Fuel Cell Anodes. *ACS Catal.* **2013**, *3*, 1801−1809.

(11) Monte, R. D.; Kašpar, J. On the Role of Oxygen Storage in Three-Way Catalysis. *Top. Catal.* **2004**, *28*, 47−57.

(12) Tada, S.; Shimizu, T.; Kameyama, H.; Haneda, T.; Kikuchi, R. Ni/CeO_2 Catalysts with High CO_2 Methanation Activity and High CH_4 Selectivity at Low Temperatures. *Int. J. Hydrog. Energy* **2012**, *37*, 5527−5531.

(13) Boaro, M.; Colussi, S.; Trovarelli, A. Ceria-Based Materials in Hydrogenation and Reforming Reactions for CO_2 Valorization. *Front. Chem.* **2019**, *7*, 28.

(14) Su, X.; Xu, J.; Liang, B.; Duan, H.; Hou, B.; Huang, Y. Catalytic Carbon Dioxide Hydrogenation to Methane: A Review of Recent Studies. *J. Energy Chem.* **2016**, *25*, 553−565.

(15) He, L.; Fan, Y.; Bellettre, J.; Yue, J.; Luo, L. A Review on Catalytic Methane Combustion at Low Temperatures: Catalysts, Mechanisms, Reaction Conditions and Reactor Designs. *Renew. Sustain. Energy Rev.* **2020**, *119*, 109589.

(16) Guilera, J.; del Valle, J.; Alarcón, A.; Díaz, J. A.; Andreu, T. Metal-Oxide Promoted Ni/Al_2O_3 as CO_2 Methanation Micro-Size Catalysts. *J. CO_2 Util.* **2019**, *30*, 11−17.

(17) Mitchell, S.; Michels, N.-L.; Pérez-Ramírez, J. From Powder to Technical Body: The Undervalued Science of Catalyst Scale Up. *Chem. Soc. Rev.* **2013**, *42*, 6094.

(18) Jong, K. P., Ed. In *Synthesis of Solid Catalysts*; Wiley-VCH: Weinheim, 2009.

(19) Laguna, O. H.; Domínguez, M. I.; Centeno, M. A.; Odriozola, J. A. Chapter 4 - Catalysts on Metallic Surfaces: Monoliths and Microreactors. In *New Materials for Catalytic Applications*; Parvulescu, V. I., Kemnitz, E., Eds.; Elsevier: Amsterdam, 2016, pp 81−120. DOI: 10.1016/B978-0-444-63587-7.00004-4.

(20) Bogdan, E.; Michorczyk, P. 3D Printing in Heterogeneous Catalysis—The State of the Art. *Materials* **2020**, *13*, 4534.

(21) Michorczyk, P.; Hędrzak, E.; Węgrzyniak, A. Preparation of Monolithic Catalysts Using 3D Printed Templates for Oxidative Coupling of Methane. *J. Mater. Chem. A* **2016**, *4*, 18753−18756.

(22) Whiting, G. T.; Chung, S.-H.; Stosic, D.; Chowdhury, A. D.; van der Wal, L. I.; Fu, D.; Zecevic, J.; Travert, A.; Houben, K.; Baldus, M.; Weckhuysen, B. M. Multiscale Mechanistic Insights of Shaped Catalyst Body Formulations and Their Impact on Catalytic Properties. *ACS Catal.* **2019**, *9*, 4792−4803.

(23) Zhao, X.; Walker, D. M.; Maiti, D.; Petrov, A. D.; Kastelic, M.; Joseph, B.; Kuhn, J. N. NiMg/Ceria-Zirconia Cylindrical Pellet Catalysts for Tri-Reforming of Surrogate Biogas. *Ind. Eng. Chem. Res.* **2018**, *57*, 845−855.

(24) Zhao, X.; Kuhn, J. N.; Walker, D. M.; Joseph, B. Mixed Metal Oxide Extrudate Catalyst. U. S. Patent 10,618,042 B1 , 2020.

(25) Beheshti, M. S.; Behzad, M.; Ahmadpour, J.; Arabi, H. Modification of H-[B]-ZSM-5 Zeolite for Methanol to Propylene (MTP) Conversion: Investigation of Extrusion and Steaming Treatments on Physicochemical Characteristics and Catalytic Performance. *Microporous Mesoporous Mater.* **2020**, *291*, 109699.

(26) Mohr, G. D.; Verduijn, J. P. Hydrocarbon conversion using a zeolite bound zeolite catalyst, U. S. Patent 6,039,864 A , 2000.

(27) Hernando, H.; Ochoa-Hernández, C.; Shamzhy, M.; Moreno, I.; Fermoso, J.; Pizarro, P.; Coronado, J. M.; Čejka, J.; Serrano, D. P. The Crucial Role of Clay Binders in the Performance of ZSM-5 Based Materials for Biomass Catalytic Pyrolysis. *Catal. Sci. Technol.* **2019**, *9*, 789−802.

(28) Zhao, B.; Zhang, Y.; Dou, X.; Wu, X.; Yang, M. Granulation of Fe−Al−Ce Trimetal Hydroxide as a Fluoride Adsorbent Using the Extrusion Method. *Chem. Eng. J.* **2012**, *185−186*, 211−218.

(29) Devyatkov, S. Yu.; Zinnurova, A. Al.; Aho, A.; Kronlund, D.; Peltonen, J.; Kuzichkin, N. V.; Lisitsyn, N. V.; Murzin, D. Yu. Shaping of Sulfated Zirconia Catalysts by Extrusion: Understanding the Role of Binders. *Ind. Eng. Chem. Res.* **2016**, *55*, 6595−6606.

(30) Jasra, R. V.; Tyagi, B.; Badheka, Y. M.; Choudary, V. N.; Bhat, T. S. G. Effect of Clay Binder on Sorption and Catalytic Properties of Zeolite Pellets. *Ind. Eng. Chem. Res.* **2003**, *42*, 3263−3272.

(31) Velthoen, M. E. Z.; Lucini Paioni, A.; Teune, I. E.; Baldus, M.; Weckhuysen, B. M. Matrix Effects in a Fluid Catalytic Cracking Catalyst Particle: Influence on Structure, Acidity, and Accessibility. *Chem. − Eur. J.* **2020**, *26*, 11995−12009.

(32) Lari, G. M.; de Moura, A. B. L.; Weimann, L.; Mitchell, S.; Mondelli, C.; Pérez-Ramírez, J.; Pérez-Ramírez, J. Design of a Technical Mg−Al Mixed Oxide Catalyst for the Continuous Manufacture of Glycerol Carbonate. *J. Mater. Chem. A* **2017**, *5*, 16200−16211.

(33) Whiting, G. T.; Meirer, F.; Mertens, M. M.; Bons, A.-J.; Weiss, B. M.; Stevens, P. A.; de Smit, E.; Weckhuysen, B. M. Binder Effects

in SiO_2- and Al_2O_3-Bound Zeolite ZSM-5-Based Extrudates as Studied by Microspectroscopy. *ChemCatChem* **2015**, *7*, 1312−1321.
(34) Luna-Murillo, B.; Pala, M.; Paioni, A. L.; Baldus, M.; Ronsse, F.; Prins, W.; Bruijnincx, P. C. A.; Weckhuysen, B. M. Catalytic Fast Pyrolysis of Biomass: Catalyst Characterization Reveals the Feed-Dependent Deactivation of a Technical ZSM-5-Based Catalyst. *ACS Sustain. Chem. Eng.* **2021**, *9*, 291−304.
(35) Maca, K.; Trunec, M.; Cihlar, J. Injection Moulding and Sintering of Ceria Ceramics. *Ceram. Int.* **2002**, *28*, 337−344.
(36) Guesnet, L.; Bassat, J. M.; Grenier, J. C.; Chartier, T.; Geffroy, P.-M. Shaping of Ceria-Based Single Solid Oxide Cells Combining Tape-Casting, Screen-Printing and Infiltration. *J. Eur. Ceram. Soc.* **2020**, *40*, 5662−5669.
(37) Vendrell, X.; Kubyshin, Y.; Mestres, L.; Llorca, J. CO Oxidation on Ceria Studied by Electrochemical Impedance Spectroscopy. *ChemCatChem* **2020**, *12*, 5926−5931.
(38) Zyryanova, M. M.; Snytnikov, P. V.; Amosov, Yu. I.; Kuzmin, V. A.; Kirillov, V. A.; Sobyanin, V. A. Design, Scale-out, and Operation of a Preferential CO Methanation Reactor with a Nickel−Ceria Catalyst. *Chem. Eng. J.* **2011**, *176*−*177*, 106−113.
(39) Blanchard, G.; Quemere, E. Composition Based on Cerium Oxide or on Cerium and Zirconium Oxides, in the Extruded Form, Process for the Preparation Thereof and Use Thereof as Catalyst. U. S. Patent 6,506,705 B2 , 2003.
(40) Lucentini, I.; Serrano, I.; Soler, L.; Divins, N. J.; Llorca, J. Ammonia Decomposition over 3D-Printed CeO_2 Structures Loaded with Ni. *Appl. Catal. Gen.* **2020**, *591*, 117382.
(41) Benbow, J. J.; Oxley, E. W.; Bridgwater, J. The extrusion mechanics of pastes − the influence of paste formulation on extrusion parameters. *Chem. Eng. Sci.* **1987**, *42*, 2151−2162.
(42) Händle, F. *Extrusion in Ceramics*; Springer, 2007.
(43) Porta, A.; Falbo, L.; Visconti, C. G.; Lietti, L.; Bassano, C.; Deiana, P. Synthesis of Ru-Based Catalysts for CO_2 Methanation and Experimental Assessment of Intraporous Transport Limitations. *Catal. Today* **2020**, *343*, 38−47.
(44) Middelkoop, V.; Vamvakeros, A.; de Wit, D.; Jacques, S. D. M.; Danaci, S.; Jacquot, C.; de Vos, Y.; Matras, D.; Price, S. W. T.; Beale, A. M. 3D Printed Ni/Al_2O_3 Based Catalysts for CO_2 Methanation - a Comparative and Operando XRD-CT Study. *J. CO_2 Util.* **2019**, *33*, 478−487.
(45) Cimino, S.; Russo, R.; Lisi, L. Insights into the Cyclic CO_2 Capture and Catalytic Methanation over Highly Performing Li-Ru/Al_2O_3 Dual Function Materials. *Chem. Eng. J.* **2022**, *428*, 131275.
(46) Alarcón, A.; Guilera, J.; Díaz, J. A.; Andreu, T. Optimization of Nickel and Ceria Catalyst Content for Synthetic Natural Gas Production through CO_2 Methanation. *Fuel Process. Technol.* **2019**, *193*, 114−122.
(47) Lau, C. L. S.; Yu, Q.; Lister, V. Y.; Rough, S. L.; Wilson, D. I.; Zhang, M. The Evolution of Pellet Size and Shape during Spheronisation of an Extruded Microcrystalline Cellulose Paste. *Chem. Eng. Res. Des.* **2014**, *92*, 2413−2424.
(48) Sing, K. S. W.; Everett, D. H.; Haul, R. A. W.; Moscou, L.; Pierotti, R. A.; Rouquerol, J.; Siemieniewska, T. Repoting physisorption data for gas/solid systems with special reference to the determination of surface area and porosity. *Pure Appl. Chem.* **1985**, *57*, 603−619.
(49) Patnaik, P.. *Handbook of Inorganic Chemicals*, 1 edition.; McGraw-Hill Professional, 2002.
(50) Pino, L.; Vita, A.; Cipitì, F.; Laganà, M.; Recupero, V. Catalytic Performance of $Ce_{1-x}Ni_xO_2$ Catalysts for Propane Oxidative Steam Reforming. *Catal. Lett.* **2008**, *122*, 121−130.
(51) Trovarelli, A. Catalytic Properties of Ceria and CeO_2-Containing Materials. *Catal. Rev.* **1996**, *38*, 439−520.
(52) Gao, J.; Jia, C.; Li, J.; Zhang, M.; Gu, F.; Xu, G.; Zhong, Z.; Su, F. Ni/Al_2O_3 Catalysts for CO Methanation: Effect of Al_2O_3 Supports Calcined at Different Temperatures. *J. Energy Chem.* **2013**, *22*, 919−927.
(53) Barrault, J.; Alouche, A.; Paul-Boncour, V.; Hilaire, L.; Percheron-Guegan, A. Influence of the Support on the Catalytic Properties of Nickel/Ceria in Carbon Monoxide and Benzene Hydrogenation. *Appl. Catal.* **1989**, *46*, 269−279.
(54) Guilera, J.; Boeltken, T.; Timm, F.; Mallol, I.; Alarcón, A.; Andreu, T. Pushing the Limits of SNG Process Intensification: High GHSV Operation at Pilot Scale. *ACS Sustain. Chem. Eng.* **2020**, *8*, 8409−8418.
(55) Velu, S.; Gangwal, S. Synthesis of Alumina Supported Nickel Nanoparticle Catalysts and Evaluation of Nickel Metal Dispersions by Temperature Programmed Desorption. *Solid State Ionics* **2006**, *177*, 803−811.
(56) Zhang, Z.; Wei, T.; Chen, G.; Li, C.; Dong, D.; Wu, W.; Liu, Q.; Hu, X. Understanding Correlation of the Interaction between Nickel and Alumina with the Catalytic Behaviors in Steam Reforming and Methanation. *Fuel* **2019**, *250*, 176−193.
(57) Bengaouer, A.; Ducamp, J.; Champon, I.; Try, R. Performance Evaluation of Fixed-Bed, Millistructured, and Metallic Foam Reactor Channels for CO $_2$ Methanation. *Can. J. Chem. Eng.* **2018**, *96*, 1937−1945.
(58) Guilera, J.; Andreu, T.; Basset, N.; Boeltken, T.; Timm, F.; Mallol, I.; Morante, J. R. Synthetic Natural Gas Production from Biogas in a Waste Water Treatment Plant. *Renewable Energy* **2020**, *146*, 1301−1308.
(59) Farsi, S.; Liang, S.; Pfeifer, P.; Dittmeyer, R. Application of Evaporation Cooling in a Microstructured Packed Bed Reactor for Decentralized CO_2 Methanation. *Int. J. Hydrog. Energy* **2021**, *46*, 19971−19987.
(60) Kobl, K.; Angelo, L.; Zimmermann, Y.; Sall, S.; Parkhomenko, K.; Roger, A.-C. In Situ Infrared Study of Formate Reactivity on Water−Gas Shift and Methanol Synthesis Catalysts. *Comptes Rendus Chim* **2015**, *18*, 302−314.
(61) Pan, Q.; Peng, J.; Sun, T.; Wang, S.; Wang, S. Insight into the Reaction Route of CO_2 Methanation: Promotion Effect of Medium Basic Sites. *Catal. Commun.* **2014**, *45*, 74−78.
(62) Vayssilov, G. N.; Mihaylov, M.; Petkov, P. St.; Hadjiivanov, K. I.; Neyman, K. M. Reassignment of the Vibrational Spectra of Carbonates, Formates, and Related Surface Species on Ceria: A Combined Density Functional and Infrared Spectroscopy Investigation. *J. Phys. Chem. C* **2011**, *115*, 23435−23454.
(63) Cárdenas-Arenas, A.; Quindimil, A.; Davó-Quiñonero, A.; Bailón-García, E.; Lozano-Castelló, D.; De-La-Torre, U.; Pereda-Ayo, B.; González-Marcos, J. A.; González-Velasco, J. R.; Bueno-López, A. Isotopic and in Situ DRIFTS Study of the CO_2 Methanation Mechanism Using Ni/CeO_2 and Ni/Al_2O_3 Catalysts. *Appl. Catal. B Environ.* **2020**, *265*, 118538.
(64) Alarcón, A.; Guilera, J.; Andreu, T. An Insight into the Heat-Management for the CO_2 Methanation Based on Free Convection. *Fuel Process. Technol.* **2021**, *213*, 106666.
(65) Moioli, E.; Gallandat, N.; Züttel, A. Model Based Determination of the Optimal Reactor Concept for Sabatier Reaction in Small-Scale Applications over Ru/Al_2O_3. *Chem. Eng. J.* **2019**, *375*, 121954.
(66) Vasheghani, M.; Marzbanrad, E.; Zamani, C.; Aminy, M.; Raissi, B.; Ebadzadeh, T.; Barzegar-Bafrooei, H. Effect of Al_2O_3 Phases on the Enhancement of Thermal Conductivity and Viscosity of Nanofluids in Engine Oil. *Heat Mass Transfer* **2011**, *47*, 1401−1405.
(67) Suzuki, K.; Kato, M.; Sunaoshi, T.; Uno, H.; Carvajal-Nunez, U.; Nelson, A. T.; McClellan, K. J. Thermal and Mechanical Properties of CeO_2. *J. Am. Ceram. Soc.* **2019**, *102*, 1994−2008.

https://doi.org/10.1021/acsaenm.2c00214
ACS Appl. Eng. Mater. 2023, 1, 1106−1115